SIMULATIONS OF THE LARGE-SCALE STRUCTURE FORMATION AND THE EVOLUTION OF THE LYMAN ALPHA FOREST: COMPARISON WITH OBSERVATIONS

J.P. MÜCKET AND R. RIEDIGER
Astrophysikalisches Institute Potsdam
An der Sternwarte 16, D-14482 Potsdam, Germany

AND

P. PETITJEAN[1,2]
[1] *Institut d'Astrophysique de Paris - CNRS*
98bis Boulevard Arago, F-75014 Paris, France
[2] *UA CNRS 173- DAEC, Observatoire de Paris-Meudon*
F-92192 Meudon Principal Cedex, France

1. Introduction

The study of the Lyα absorbers seen in quasar spectra is a very sensitive way to probe the baryonic material in the whole redshift range $0 < z < 5$. In particular the evolution of the spatial distribution of the Lyα clouds offers the unique chance to obtain direct information about the structure formation processes throughout a wide redshift range. During recent years considerable success has been obtained in modeling the distribution of the neutral hydrogen gas in the context of the evolution of large-scale structure (Cen *et al.* 1994, Petitjean *et al.* 1995, Mücket *et al.* 1996, Hernquist *et al.* 1996, Miralda-Escudé *et al.* 1996, Zhang *et al.* 1996, Bi & Davidsen 1996) By means of simulations many of the characteristics of the Lyα forest could be reproduced. One of the outstanding problems is the relation between the Lyman-α forest and galaxies. Although conclusions are uncertain, it seems that at least the strongest lines in the Lyman-α forest at low redshift are anyhow associated with galaxies (Lanzetta *et al.* 1995, Le Brun *et al.* 1996) since the density of the intergalactic gas is expected to be higher in the vicinity of the galactic potential wells. The case for the weak line to be associated with galaxies is less clear. Indeed observations of the line of sight to 3C273 that are the most sensitive to the presence of weak lines

(Morris *et al.* 1991, Bahcall *et al.* 1991) indicate the presence of a large number of these lines and no clear association with galaxies is seen (Morris *et al.* 1993). Moreover, Stocke *et al.* (1995) have detected weak absorption lines located in regions devoided of galaxies.

Recent observations have shown that at redshift $z \sim 3$, CIV is found in 90% of the clouds with $N(\mathrm{HI}) > 10^{15}$ cm^{-2} and in about 50% of the clouds with 3×10^{14} cm$^{-2} < N(\mathrm{HI}) < 10^{15}$ cm^{-2} (Songaila & Cowie 1996, Cowie *et al.* 1995).

Following the simulations the Lyman-α absorption line properties can be understood if the gas traces the development of structures in the Universe. In this picture, part of the gas is located inside filaments where star formation can occur very early in small halos that subsequently merge to build-up a so-called galaxy (Haehnelt *et al.* 1996). This gas contains metals. The remaining part of the gas has very low metallicity or no metals and either is loosely associated with the filaments and has $N(\mathrm{HI}) \geq 10^{14}$ cm^{-2} or is located in the underdense regions and has $N(\mathrm{HI}) \leq 10^{14}$ cm^{-2}.

To clarify this issue, we have refined our simulations introducing a distinction between shocked and unshocked particles leading in the result, as will be shown, to two different populations of Lyman-α clouds.

2. Simulations

We described in Mücket *et al.* (1996) the main characteristics of a pseudo-hydrodynamic code using the particle-mesh (PM) code developed by Kates *et al.* (1991) including temperature evolution of the gas component associated with the dark matter and effects of photoionisation. The simulations used 128^3 particles on a 256^3 grid. We carefully analyzed the length scales to be assigned to the simulation box and to the cells. Taking into account the restrictions due to scales of nonlinearity at $z = 0$ and recent observations which give estimates for the cloud sizes the simulations were carried out using a box size of 12.8 Mpc which corresponds to a co-moving cell size of 50 kpc. The baryonic mass is assumed to be proportional to the dark matter mass inside a cell. This assumption has been shown by detailed hydro-simulations to be valid for the low-density regime characteristic of the Lyman-α forest (see Miralda-Escudé *et al.* 1996, Hernquist *et al.* 1996).

We adopt a value for the Hubble parameter $H_0 = 50$ km Mpc^{-1} s^{-1} and $\Omega_\mathrm{b} = 0.05$ throughout.

The photoionizing UV background flux responsible for the photoionisation is calculated by the code self-consistently and is assumed to be homogeneous and isotropic throughout the simulation box. The ionizing spectrum is modelled as $J_\nu \propto J_0\, \nu^{-1}$ where $J_0 = J_{-21} \cdot 10^{-21}$ erg cm^{-2} s^{-1} Hz^{-1} sr^{-1} is the ionizing flux at 13.6 eV which depends on redshift, *i.e.*, $J_{-21} = f(z)$.

The UV background flux is assumed to be determined by star formation processes in collapsing cool and dense regions. The variation of the flux intensity at redshift z is related to the rate $\Delta m(T_4 < 0.5; z)$ at which the baryonic material cools below $T_4 = 0.5$ (with $T = T_4 \cdot 10^4$ K) in the simulation and to the expansion of the Universe:

$$\begin{aligned} f(z) &= C_{\rm cool}\, \Delta m(T_4 < 0.5; z) \\ &\quad + f(z + \Delta z) \left(\frac{1+z}{1+z+\Delta z} \right)^4 , \end{aligned} \tag{1}$$

where $C_{\rm cool}$ is a factor of proportionality. To avoid overcooling (*e.g.*, Blanchard *et al.* 1992), we assume that the cool gas is transformed into stars with an efficiency ε of about 8%. The remainder of the gas is reheated to temperatures above 50 000 K. The characteristic time period for those processes is of order $t_* \approx 10^8$ years. This procedure provide simulation results that are independent of the time step.

Whereas the time dependence of the UV flux is almost not affected by the value of t_* within a reasonable range the actual value of the efficiency parameter has considerable influence on the flux intensity at small redshifts (see also Miralda-Escudé *et al.* 1996). Namely in this scenario it determines the amount of gas still available for star formation.

During the simulation we distinguish between two different populations of clouds: Part of matter particles are involved in shell-crossing processes (shocks). In those cases the procedure for temperature assignment proposed by Kates *et al.* (1991) can be applied:

(1) A particle is labeled "shocked" if the Jacobi determinant of the transformation from Lagrange (particle) to Euler (grid) coordinates becomes negative.

(2) If the particle enters a shocked region, defined as entering a cell on a coarse grid of cell size $2l_{\rm c}$ containing at least one shocked particle. In either case, we attempt to define a local velocity field $\mathbf{U}$ on the coarse grid, and we assign to the gas associated with the particle a temperature according to $kT = \mu_{\rm H} m_{\rm H} (\mathbf{v} - \mathbf{U})^2/3$, where $\mathbf{v}$ is the particle velocity, $\mu_{\rm H}$ the molecular weight and $m_{\rm H}$ the mass of the hydrogen atom.

We assume ionization equilibrium which is a good approximation when the gas is fully ionized (Duncan *et al.* 1989). The temperature is determined using the time dependent equations (see Mücket *et al.* 1996). The shocked particles are mostly found in big halos and elongated, filamentary structures (regions of enhanced density). The remainder of the gas is unshocked. It is found in the surroundings of the structures formed by shocked particles but mostly in the voids delineated by these structures. The gas here is photo-ionized by the background flux and assumed in thermal equilibrium.

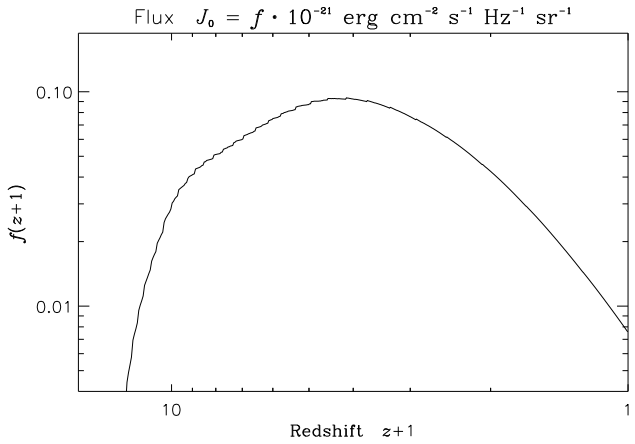

Figure 1. The UV-background flux computed in the course of our simulations.

We have monitored all results for both populations separately. The modeling of the cloud distribution along a full line of sight up to a fictitious QSO at redshift $z = 5$ is described in detail in Mücket *et al.* (1996).

3. Results

The simulation must reproduce the evolution with time of the number of Lyman-α absorption lines. Due to blending, the comparison between simulations and observations is not simple. A first constrain is thus to reproduce the evolution of the average Lyman-α decrement. As emphasized by Miralda-Escudé *et al.* (1996), this number depends on the mean HI density directly related to $J_0^{-1}(\Omega_{\rm b}h^2)^2$ where $\Omega_{\rm b}$ is the baryon density and $J_0 = J_{-21} \cdot 10^{-21}$ erg cm^{-2} s^{-1} Hz^{-1} sr^{-1} is the ionizing flux at 13.6 eV. In our simulations, the baryon density is given a value 0.05 ($\Omega_{\rm b}h^2 = 0.0125$) and the evolution with redshift of the ionizing flux is computed assuming that its variation is related to the amount of gas that collapses in the simulation at any time (see Section 2). The only free parameter is thus the normalization of $J_{-21}(z)$. A value of $J_{-21}(z_0) = 0.1$ at $z_0 \sim 3$ (see Fig. 1) fits the decrement evolution quite well (see Fig. 2).

It must be noticed, that the redshift range considered here is large ($0 < z < 5$) and the flux is significantly changing. It is thus necessary and important to calculate the variations consistently in order to be able to discuss the evolution of the Lyman-α forest over the whole redshift range.

Our result for the flux normalisation is consistent with the findings by Hernquist *et al.* (1996) and Miralda-Escudé *et al.* (1996) using hydro simulations over a much smaller redshift range.

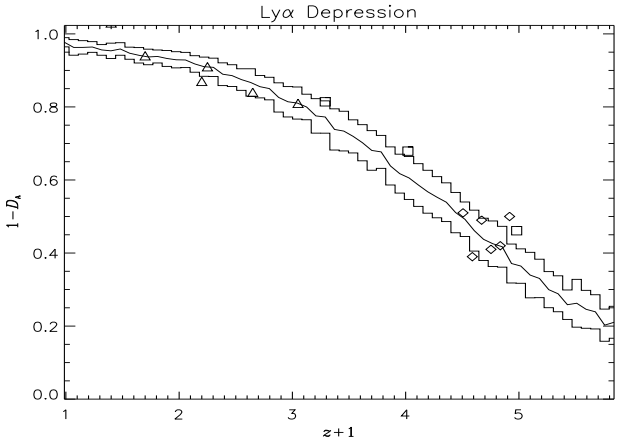

Figure 2. Lyman-α continuum depression versus redshift. Observed data are from: diamonds, Lu *et al.* (1996); triangles, a compilation by Jenkins & Ostriker (1991) at low redshifts; squares: Rauch *et al.* (1997).

Fitting the Lyman-α forest is ususally done using Voigt profile deblending procedures. Even though blending is a severe limitation for this analysis at $z > 2.5$, it is interesting to compare the observed number of lines with the simulated number of clouds that is perfectly defined. For $N(\mathrm{HI}) > 10^{14}$ cm^{-2}, the lines are not numerous enough for blending to be a problem. It can be seen from Fig. 3a that the evolution of the total number of strong lines is well reproduced. Data are taken from Lu *et al.* (1991), Petitjean *et al.* (1993) and Bahcall *et al.* (1993).

If the number of lines per unit redshift is approximated by a power-law ($\mathrm{d}n/\mathrm{d}z \propto (1+z)^{\gamma}$), we find $\gamma \approx 2.6$ for $1.5 < z < 5$ and $\gamma \approx 0.6$ for $0 < z < 1.5$. The simulated number is also consistent with observation at $z > 4$ (Williger *et al.* 1994).

Fig. 3b shows the contributions of the two populations of clouds with $N(\mathrm{HI}) > 10^{14}$ cm^{-2}, shocked (solid line) and unshocked (dash-dotted line). It is apparent that the dominant population is different before and after $z \sim 3$. At high redshift, most of the lines arise in unshocked particles whereas at low redshift, most of the gas is condensed in filamentary structures (see Petitjean *et al.* 1995).

Let us assume that most of the unshocked clouds are co-expanding and optically thin. If we also assume the flux to be nearly constant throughout the considered redshift range, then the evolution of the column density for each cloud is $\propto J_0^{-1} n_{\mathrm{H}}^2 l_{\mathrm{c}} \propto (1+z)^5$, *i.e.*, the column density of such clouds is a rapidly decreasing function of time. Therefore, at high redshift, a similar behavior is expected for the number density of the clouds providing

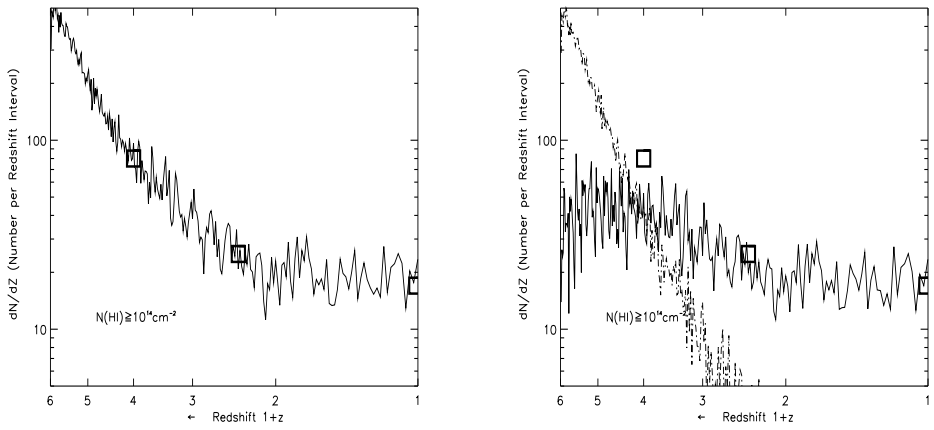

Figure 3. (a) Number density $\mathrm{d}n/\mathrm{d}z$ of clouds with column density $\log N(\mathrm{HI}) > 14$ versus redshift z. (b) As in (a). The number density of lines drawn from the shocked and unshocked populations are plotted as full and dash-dotted lines respectively

a column density threshold is given. That might explain the very steep slope found for the number density evolution of the unshocked clouds as shown in Fig. 3b.

The number density of lines with $N(\mathrm{HI}) > 10^{12}$ cm^{-2} is about constant over the redshift range $1 < z < 5$ (see Fig. 5 and decreases slowly at lower redshift. Low density gas is found in regions delineated by filamentary and sheet-like structures at high redshift. This gas slowly disappears. The total number density of lines stays constant because the high column density gas has column density decreasing with time. Such a difference in the evolution of the number density of weak and strong lines, although to be confirmed, has been noticed in intermediate resolution data (Bechtold 1994). Fig. 8 gives a visual impression of the distributions of clouds having column densities within the range 10^{14} cm$^{-2} < N(\mathrm{HI} < 10^{14}$ cm^{-2} at different redshifts. Most of the clouds seen at $z = 3$ are distributed in sheet-like and filamentary structures are not longer detectable at this column density range at $z = 1$ or even $z = 0$. For the fixed density threshold $N(\mathrm{HI} \approx 10^{14}$ cm^{-2} the detectable structures in the HI distribution are transformed from sheet-like to filamentary and eventually to single clumpy structures.

Fig. 4 shows an example for a simulated full spectrum along a single line of sight at a resolution similar to Keck HIRES observations. The absorption features are calculated from the parameters obtained for each cell in the simulation. The line number density is calculated as in Mücket *et al.* (1996). The resulting HI column density distribution is given in Fig. 6 (solid line) together with the observed points taken from Hu *et al.* (1996).

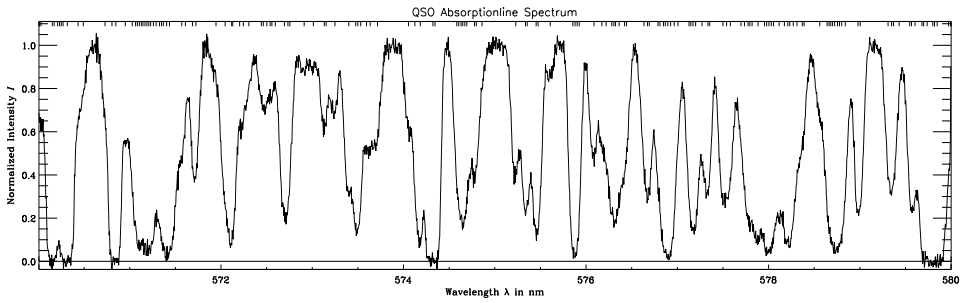

Figure 4. Part of a synthetic spectrum derived from simulation data along a single line of sight.

The agreement is good for column densities $N(\mathrm{HI}) \geq 10^{14}$ cm^{-2}. In this range the distribution is dominated by the contribution from shocked particles (dotted line). For lower column densities the distribution is dominated by the contribution from the unshocked particles (dashed line) and is too large by a factor of two compared to observations. However this factor is well within the uncertainty of both observational and simulated data. The discrepancy could result from the limited resolution of simulations. A flattening is apparent toward lower column densities. The comparison of the column density distributions at different redshifts shows that the flattening happens at larger N for higher redshifts in agreement with the predictions by Mücket *et al.* 1996 (cp. Eq. 7). So the onset of the flattening at small column densities is related to the resolution of the simulations. On the other hand, the behavior is similar to that recently observed at redshifts $z \approx 3 \ldots 4$ that is usually attributed to the blending of weak lines with stronger ones.

The lines are considered broadened by thermal and turbulent motions. The thermal broadening is derived from the temperature. The turbulent broadening is estimated as the root mean square of peculiar velocities in one cell. The resulting distribution together with data from Lu *et al.* (1996) is shown in Fig. 7. There is a lack of small Doppler parameters in both the observed and and simulated data. The mean temperature of the gas beeing 20 000 K, this means that broadening of the lines is dominated by turbulent motions. Note that this procedure does not apply to unshocked particles since the number of particles within one cell is too small to define turbulent motions this way. A weak dependence of the Doppler parameter distribution with redshift is observed in the simulations: The maximum of the distribution is marginally shifted to higher Doppler parameters with decreasing redshift.

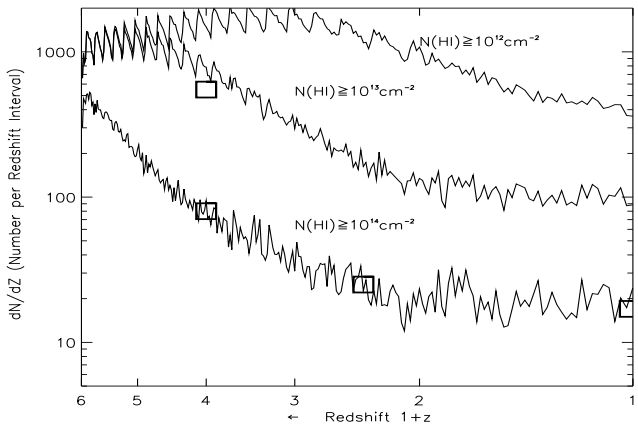

Figure 5. Number density of lines versus redshift for different column densities thresholds $\log N(\mathrm{HI}) > 12, 13, 14$.

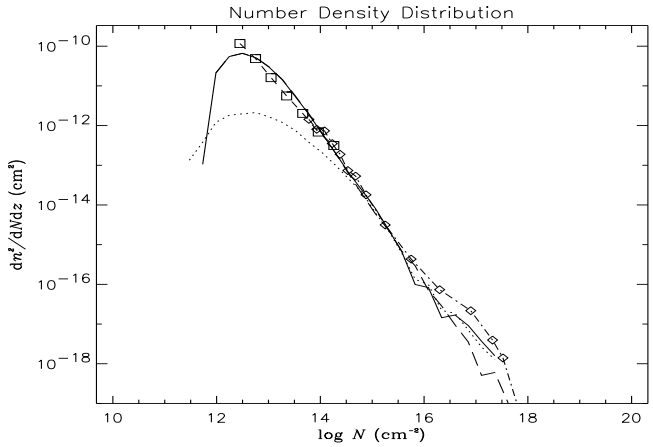

Figure 6. H I column density distribution at $z = 3$ for the shocked particles (dotted line), the unshocked particles (dashed line) and all the particules together (solid line). Observational data points from Hu *et al.* (1995) and Petitjean *et al.* (1993) are indicated by square symbols.

4. Conclusion

We have refined our simulations (Mücket *et al.* 1996) introducing a distinction between shocked particles predominantly found within dense structures such as filaments and unshocked particles which populate underdense regions.

At redshifts $z < 2.5$ the number density of lines arising from unshocked

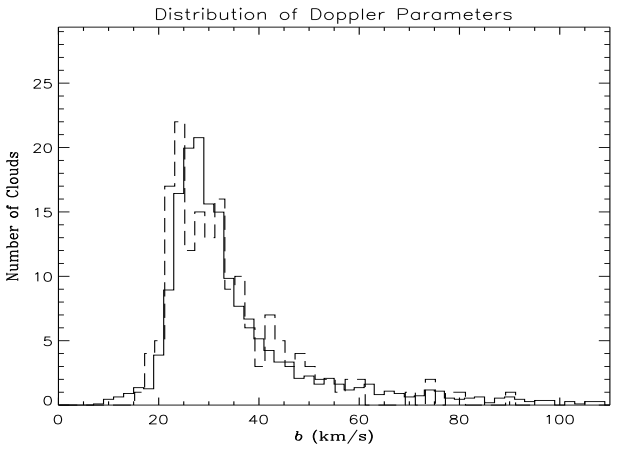

Figure 7. Doppler parameter distribution (solid line). Results from Lu *et al.* (1996) are overplotted as a dashed line.

particles decreases very rapidly for H I column densities larger than 10^{14} cm^{-2}. Therefore at low redshifts, the main contribution for this column density threshold comes from shocked particles. As mentioned above early star formation probably occurs in the filamentary structures and most of the Lyman-α clouds with column densities $\log N(\mathrm{HI}) > 14$ are expected to contain metals. In addition a large fraction of those clouds at low redshift should somehow be correlated with galaxies (Petitjean *et al.* 1995).

The number density of lines with $\log N(\mathrm{HI}) > 12$ remains about constant over the redshift range $5 > z > 1$ and decreases slowly at lower redshift. This is the result of both decreasing ionizing flux and mean hydrogen density. The number density of such weak lines is predicted to be larger than 200 per unit redshift at $z \sim 0$. This prediction can be tested along the line of sight to 3C273 with the new instrumentation to be installed on the Hubble Space Telescope.

Determination of realistic Doppler parameters for clouds in the underdense regions needs consideration of sub-cellular effects. The internal velocity and temperature distribution for one-particle clouds is thus beyond the limit of our simulations. However the contribution of the shocked particles alone yields a Doppler parameter distribution in reasonable agreement with observations.

Our simulation yields a consistent determination of the evolution of the UV flux intensity over the whole redshift range $0 < z < 5$ (see Fig. 1). The normalisation is obtained by fitting the Lyman-α decrement; a value of $J_{-21}(z_0) = 0.1$ at $z_0 \sim 3$ fits the decrement evolution quite well (see Fig. 2) for $\Omega_{\mathrm{b}} h^2 \sim 0.0125$.

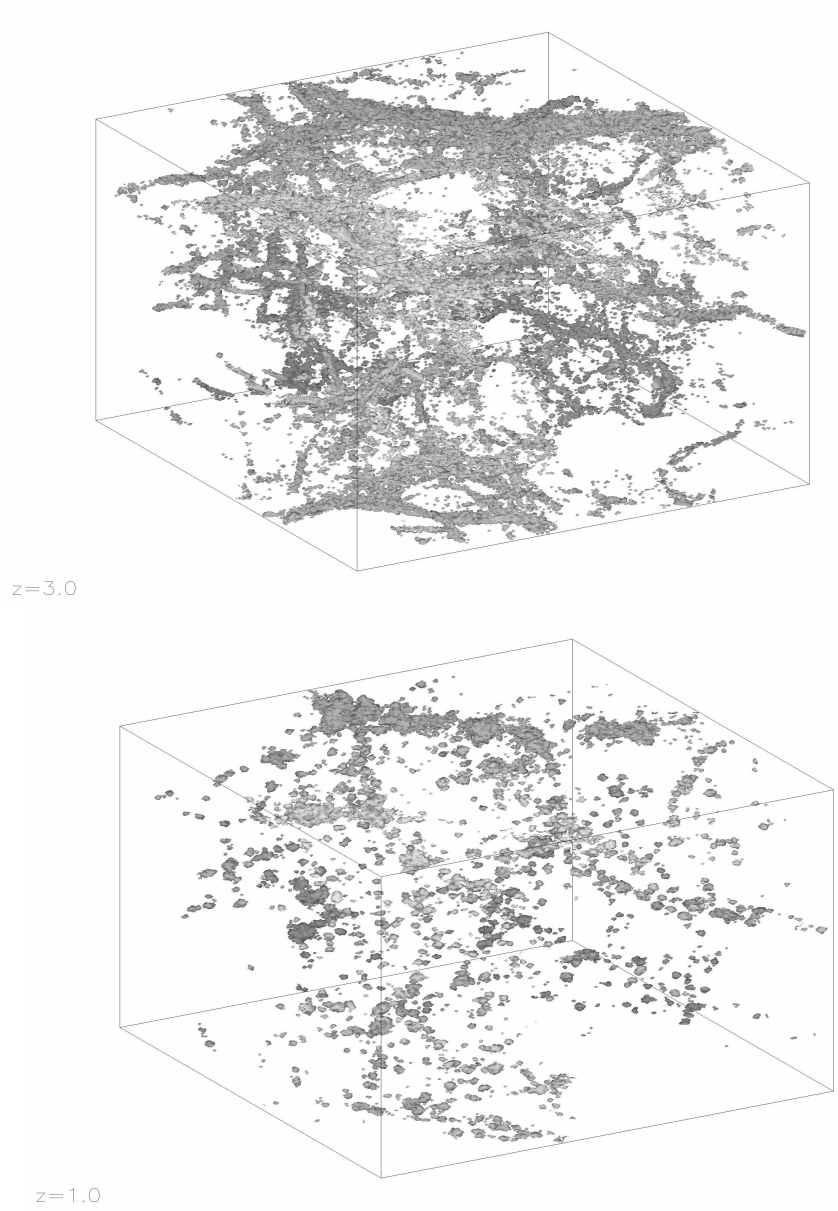

Figure 8. The distribution of HI clouds having column densities within the range $14 < \log_{10}(NHI/cm^{-2}) < 16$ at the epochs z=3 and z=1. The box length is 12.8 Mpc.

References

Bahcall J.N., Bergeron J., Boksenberg A., *et al.*, 1993, *ApJS* **87**, 1
Bahcall J.N., Januzzi B.T., Schneider D.P., *et al.*, 1991, *ApJL* **377**, 5
Bechtold J., 1994, *ApJS* **91**, 1
Bi HongGuang, Davidsen A.F., 1996, astro-ph/9611062
Blanchard A., Valls-Gabaud D., Mamon G.A., 1992, A&A **264**, 365
Cen R., Miralda-Escudé J., Ostriker J.P., Rauch M., 1994, *ApJL* **437**, L9
Cowie L.L., Songaila A., Kim Tae-Sun, Hu E.M., 1995, *AJ* **109**, 1522
Duncan R.C., Ostriker J.P., Bajtlik S., 1989, *ApJ* **345**, 39
Haehnelt M.G., Rauch M., Steinmetz M., 1996, *MNRAS* (in press)
Hernquist L., Katz N., Weinberg D.H., Miralda-Escudé J., 1996, *ApJ* **457**, L51
Hu E.M., Kim Tae-Sun, Cowie L.L., Songaila A., Rauch M., 1995,*AJ* **110**, 1526
Jenkins E.B., Ostriker J.P., 1991, *ApJ* **376**, 33
Kates R.E., Kotok E.V., Klypin A.A., 1991, *A&A* **243**, 295
Lanzetta K.M., Bowen D.V., Tytler D., Webb J.K., 1995, *ApJ* **442**, 538
Le Brun V., Bergeron J., Boissé P., 1996, *A&A* **306**, 691
Lu L., 1991, *ApJ* **379**, 99
Lu L., Sargent W.L.W., Womble D.S., Takada-Hidai M., 1996, *ApJ* **472**, 509
Miralda-Escudeé J., Cen R., Ostriker J.P., Rauch M., 1996, *ApJ* **471**, 582
Morris S.L., Weymann R.J., Dressler A., *et al.*, 1993, *ApJ* **419**, 524
Morris S.L., Weymann R.J., Savage B.D., Gilliland R.L., 1991, *ApJL* **377**, 21
Mücket J.P., Petitjean P., Kates R., Riediger R., 1996, *A&A* **308**, 17
Petitjean P., Bergeron J., 1994, *A&A* **283**, 759
Petitjean P., Mücket J., Kates R.E., 1995, *A&A* **295**, L9
Petitjean P., Webb J.K., Rauch M., *et al.*, 1993, *MNRAS* **262**, 499
Rauch M., Miralda-Escude J., Sargent W.L.W., Barlow T.A., Weinberg D.H., Hernquist L., Katz N., Cen R., Ostriker J.P., 1997, astro-ph/9612245
Songaila A., Cowie L.L., 1996, astro-ph/9605102
Stocke J.T., Shull J.M., Penton S., *et al.*, 1995, *ApJ* **451**, 24
Williger G.M., Baldwin J.A., Carswell R.F., *et al.*, 1994, *ApJ* **428**, 574
Zhang Yu, Meiksin A., Anninos P., Norman M.L., 1996, astro-ph/9601130